Laser powder bed fusion at sub-atmospheric pressures

Bidare, P.; Bitharas, I.; Ward, R. M.; Attallah, M. M.; Moore, A. J.

DOI:
10.1016/j.ijmachtools.2018.03.007

Document Version
Publisher's PDF, also known as Version of record

Citation for published version (Harvard):
Bidare, P, Bitharas, I, Ward, RM, Attallah, MM & Moore, AJ 2018, 'Laser powder bed fusion at sub-atmospheric pressures', *International Journal of Machine Tools and Manufacture*, vol. 130-131, pp. 65-72. https://doi.org/10.1016/j.ijmachtools.2018.03.007

International Journal of Machine Tools and Manufacture 130–131 (2018) 65–72

Contents lists available at ScienceDirect

International Journal of Machine Tools and Manufacture

journal homepage: www.elsevier.com/locate/ijmactool

Laser powder bed fusion at sub-atmospheric pressures

P. Bidare[a,*], I. Bitharas[a], R.M. Ward[b], M.M. Attallah[b], A.J. Moore[a]

[a] Institute of Photonics and Quantum Sciences, Heriot-Watt University, Edinburgh, EH14 4AS, UK
[b] School of Metallurgy and Materials, University of Birmingham, Birmingham, B15 2TT, UK

ARTICLE INFO

Keywords:
High-speed imaging
Laser powder bed fusion
Sub-atmospheric pressure
Vacuum

ABSTRACT

The perceived advantages of laser powder bed fusion (PBF) at reduced pressure include a more stable melt pool and reduced porosity. In this study, high-speed imaging was used to investigate the interaction of the laser beam with the powder bed at sub-atmospheric pressures. At atmospheric pressure, the laser plume produces a flow in the ambient atmosphere that entrains particles toward the melt pool. As the pressure decreases, this hydrodynamic entrainment increases but eventually the expansion of the laser plume prevents the particles reaching the melt pool: profiles and cross-sections of the track reveal a drastic reduction in its cross-sectional area. As the pressure decreases further, into the molecular flow regime, particles are only repelled by the plume away from the melt pool. The regime between 1 bar and ~50 mbar (the threshold pressure at which the penetration depth no longer increases) could provide a window for successful processing but might require a pre-sinter to maintain the integrity of the powder bed. Lower pressures would definitely require a pre-sinter, for which the additional processing time and increase in process complexity might be justified for porosity-critical applications.

1. Introduction

Metal powder bed fusion (PBF) is an additive manufacture process in which thermal energy selectively fuses regions of a powder bed [1]. In laser PBF, a focussed laser beam melts each powder layer in an inert atmosphere (typically argon) at or very close to atmospheric pressure. The process is sometimes referred to by manufacturers' names, for example selective laser melting (SLM) and direct metal laser sintering (DMLS). Production components can be manufactured by commercial PBF systems, but generally require part-specific process settings to be determined in order to control thermally-induced residual stresses and defects. Therefore, understanding and improving the PBF process is an active area of research to increase productivity.

A small number of researchers have begun to investigate laser PBF of metals at sub-atmospheric pressures [[2],[3],[4],[5]]. The stated advantages of sub-atmospheric pressure include reduced porosity and surface roughness in the fabricated part, similar to that achieved with laser welding: any pores that do remain would not be filled with shield gas and could therefore be removed more effectively by hot isostatic pressing. Other potential advantages stated by these authors include reduced oxidation and the control of crystal orientation. These papers describe initial studies on single powder layers: the pressure and laser settings required for a successful process have not been established and no multi-layer builds were undertaken. Indeed, the process settings reported in these papers are somewhat contradictory as described next.

Zhang et al. melted single layers of pure Ti powder with a fibre laser at 100 μbar [2]. At this single pressure, the authors varied the laser power and scan speed and found acceptable density (close to 100%) and surface porosity only at very low scan speeds, ≤0.02 m/s. The density was already reduced to 95% at a laser scan speed of 0.1 m/s, decreasing steadily to 70% at 0.6 m/s. The width and height of a single melted track were both significantly reduced, which was attributed to increased metal vaporization due to the reduction in boiling temperature at low pressure. The authors claimed that balling was completely avoided at low pressure.

In a subsequent publication, the same group scanned single tracks in stainless steel powder and investigated the effect of reducing the chamber pressure from 1 bar to 1 mbar whilst again varying the laser scan speed [3]. This time, consolidated tracks were only observed at pressures ≥100 mbar for 0.1 m/s scan speed: below 100 mbar, no powder was consolidated and only re-melting of the solid substrate occurred. The lack of powder consolidation below 100 mbar was again explained in terms of increased metal vaporization due to the reduced vaporization temperature at low pressure. The authors concluded that reduced pressure requires an increase in scan speed (or a decrease in laser power) to limit material vaporization. The apparent contradiction with their previous observations [2] at 100 μbar and low scan speeds was not addressed.

Sato et al. [4] melted single layers of Ti-6Al-4V powder on to stainless steel substrates at 50 nbar. At a very low scan speed of 10 mm/

* Corresponding author.
E-mail address: p.bidare@hw.ac.uk (P. Bidare).

https://doi.org/10.1016/j.ijmachtools.2018.03.007
Received 16 January 2018; Received in revised form 26 March 2018; Accepted 28 March 2018
Available online 01 April 2018

s, they observed a surface roughness (R_a = 0.40 μm) which was significantly lower than the most abundant powder diameter of 35 μm and the largest powder diameter of 88 μm. Imaging at 60 frames per second (fps) revealed that no spatter was produced from the melt pool at this low scan speed. At 100 mm/s, the surface roughness (R_a = 25 μm) and spatter had both increased to resemble the PBF process more closely. The authors concluded that, at sub-atmospheric pressures, the sputter free process at low laser scan speeds improves the surface roughness.

Matthews et al. [5] investigated the depletion of metal powder particles (denudation) in the zone immediately surrounding the solidified track, which can affect the porosity and surface roughness of built parts. The width of the denuded region was measured after scanning laser tracks across layers of Ti-6Al-4V powder in a vacuum chamber. The width increased as the pressure was reduced from 1 bar down to 13 mbar, and was attributed to the increased velocity of the evaporation plume from the melt pool and the associated increase in particles entrained towards the melted track by the inward flow of the ambient gas. The width then decreased from 13 mbar to a local minimum at 3 mbar, before increasing again as the pressure was further reduced to 660 μbar. The decrease and subsequent increase in the denuded zone width was attributed to the onset of molecular (or rarified) flow and the outward expansion of the evaporation plume counteracting and eventually dominating any inward flow of the ambient gas. An alternative explanation involved asymmetrical heating of particles close to the laser spot which were then propelled away by the vapour flux generated, transferring momentum to remove adjacent powder particles. However, this second explanation was not preferred because smaller diameter particles were preferentially removed below 3 mbar, whereas asymmetrical heating should affect particles of all diameters equally. High-speed images were recorded close to the melt pool at atmospheric pressure using a localized jet of inert gas, and so this mechanism at lower pressures was not confirmed.

Laser welding at sub-atmospheric pressure is well established in the literature [6] and has received increased attention recently for joining thick materials using solid state fibre and disk lasers. The penetration of a keyhole weld is typically twice that achieved at atmospheric pressure, with an associated reduction in voids in the weld seam and an increase in weld pool stability. The deep, narrow weld is similar to that achieved with electron beam welding but without the production of harmful x-rays associated with that technique. The improved penetration at reduced pressure is attributed to two principal effects: the reduction in the metal vaporization temperature, so that less energy is required to create and maintain the keyhole; and the increase in laser energy reaching the workpiece due to reduced absorption and scattering of the beam by the atmosphere. These two effects are discussed in more detail in following two paragraphs. Clearly it is not necessarily the objective to introduce a keyhole during PBF, but the effects of laser processing at sub-atmospheric pressures are informative for this study.

In laser welding, the keyhole depth increases as the ambient pressure decreases [6,7] due to the decrease in vaporization temperature at reduced pressure: the mean temperature of the molten keyhole surface is reduced [8] so that the same incident laser power is absorbed along the surface of a deeper keyhole. The penetration depth becomes independent of the ambient pressure below some threshold pressure. This effect has been explained in terms of the total pressure acting inside the keyhole to keep it open, which is the sum of the atmospheric pressure, surface tension, hydrostatic pressure and weld speed pressure [8]. Ignoring the relatively small contribution from the hydrostatic pressure, the lowest pressure that can exist in the keyhole occurs for low weld speeds under a complete vacuum and is the pressure P_C due to the surface tension only. Hence reducing the atmospheric pressure below ~ P_c/10 has no noticeable effect on the penetration depth. At sub-atmospheric pressures, the reduced vaporization temperature accounts for ~40% of the increase in penetration depth seen in laser welding [7,8].

Absorption of the incident laser beam in the laser evaporation plume (metal vapour and plasma) occurs via the inverse Bremsstrahlung process. The improved penetration depth at reduced pressure for CO_2 lasers operating at a wavelength $\lambda \sim 10$ μm has been explained in terms of reduced inverse Bremsstrahlung absorption [9]. The lower temperature of the vapour plume, combined with its reduced density, reduced the degree of ionization to the extent that the plasma was almost completely suppressed at low pressure. However, the solid state fibre and disk lasers used for welding and PBF operate at $\lambda \sim 1$ μm. They produce weakly ionized plasmas (< 5%) and the inverse Bremsstrahlung absorption, which varies with λ^2, is therefore 100 times less significant than for a CO_2 laser. Kawahito et al. measured the attenuation of a probe laser beams propagating through the laser plume above a keyhole [10] and showed that it scaled with λ^{-4}. They therefore concluded that Rayleigh scattering dominates due to small particles of condensed metallic atoms with diameter ~100 nm, at least in the plume above the keyhole; neither Mie scattering from larger agglomerations of condensation particles (which has no λ dependence) nor inverse Bremsstrahlung absorption are significant. At sub-atmospheric pressures, reduced Rayleigh scattering due to the reduced density of small condensation particles accounts for an increase of 10–20% in the incident laser power [8,10]. This effect, combined with the reduced vaporization temperature discussed in the previous paragraph, accounts for the doubling of the penetration depth observed in practice.

In this paper, we report the first high-speed imaging of the interaction of the laser with the powder bed at sub-atmospheric pressures. We investigate single powder layers in order to resolve the inconsistences in the PBF literature regarding suitable process settings for sub-atmospheric pressures. We report the penetration depth obtained in PBF at these sub-atmospheric pressures in order to gain further insight into the process. Finally we discuss the implication of our findings for potential PBF in the different flow regimes encountered at sub-atmospheric pressure.

2. Experimental system

We previously reported the design and characterisation of an open-architecture PBF system for in-situ measurements [11]. For this work, the system was encased in a custom-made vacuum chamber, Fig. 1(a). A key feature of the PBF system is computer control for the automated build of fully dense components, enabling in-process measurements under realistic build conditions. However, for this study, the laser interaction with a single powder layer was investigated in order to understand the process conditions that might enable multiple layers to be built in the future.

The vacuum chamber incorporated access windows to illuminate and image the powder bed. The window for the PBF laser was an anti-reflection coated, high-vacuum viewport assembly (Thorlabs VPCH42-C) providing ~30 mm clear aperture. Similar viewport assemblies, but without anti-refection coatings on the windows, were used for white light illumination and imaging of the powder bed. These two windows were positioned asymmetrically with respect to the vertical so as to avoid direct scatter of the illumination into the camera, Fig. 1(b). The imaging window provided a top view of the powder bed with the camera angled at ~20° to the vertical. The two end windows were not used in this study.

Experiments were performed on layers of gas-atomized stainless steel 316 L powder (Renishaw PLC) with particle diameters in the range 15–45 μm and a mean diameter of 30 μm. These layers were spread on stainless steel 304 L build plates (coupons) which had been roughened by manual, circular rubbing with P400 sandpaper. The powder layer thickness for all experiments was 50 μm, determined by the height of the powder spreader above the coupon surface [11]. Individual tracks were melted with a single mode fibre laser (SPI 400 W continuous wave, 1070 nm) focussed to a spot with a Gaussian beam profile and 4Dσ diameter of 50 μm in both the x- and y-directions.

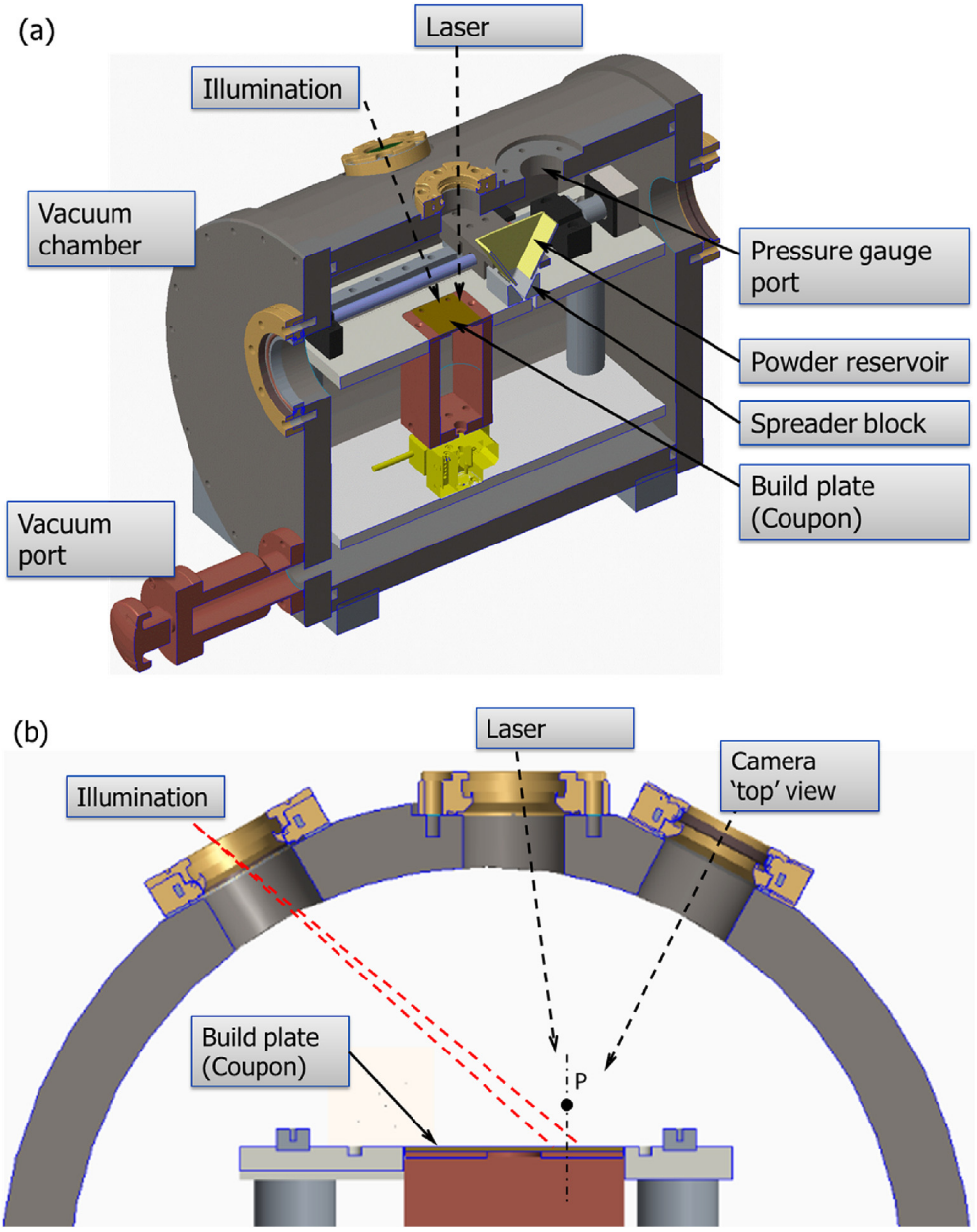

Fig. 1. (a) Schematic of the open-architecture PBF system with vacuum chamber. (b) Cross-section of the chamber showing the build area and imaging arrangement.

The vacuum port included a T-piece and isolation valves (not shown in the figure) to connect the chamber to both the vacuum pump and the Ar shield gas supply. Initially the chamber was purged with Ar by continuously filling for 10 min, with the pressure gauge port intentionally opened. Air was displaced through the pressure gauge port due to the denser Ar entering at the bottom of the chamber, a process known to reduce O_2 concentration to $< 0.1\%$ [11]. The pressure gauge (Edwards APG100-XM, NW16) was then tightened in position and the system pumped down to just below the pressure required, using an oil-free, scroll pump (Edwards XDS35i). Finally, the chamber was slowly back-filled with Ar until the required test pressure was reached. The lowest pressure tested was 10 µbar, limited by the pump performance. The pressure increase due to leakage was negligible during the time required to scan the laser tracks at a given pressure.

Image sequences were recorded with a Phantom V2512 monochrome high-speed camera. The full resolution for this camera is 1280×800 pixels up to 25,700 fps. The results reported here were recorded at 40,000 fps and 768×368 pixels. The camera was fitted with a C-mount adaptor and a QiOptiq Optem Fusion lens, configured to provide a zoom of 7:1 and a working distance of 155 mm. At this working distance, the region of interest could be varied between approximately $6 \times 8\,mm^2$ (depth of field 2.6 mm) and $0.9 \times 1.2\,mm^2$ (0.2 mm). Vignetting due to the mismatch between the 35 mm format of the camera sensor and the C-mount lens was not an issue because of the reduced image size at high frame rates. The camera was fitted with a band-stop filter to block light from the PBF laser (Thorlabs NF1064-44). The powder bed was illuminated with a white light source guided via a liquid light guide and collimator (Lumencor SOLA SM light engine) to illuminate a circle of ~10 mm diameter on the powder bed. The illumination was switched on for a few seconds during imaging and produced negligible heating of the powder bed.

3. Results

At each pressure of interest, results were recorded for three different laser power and scan speed combinations that provided the same line

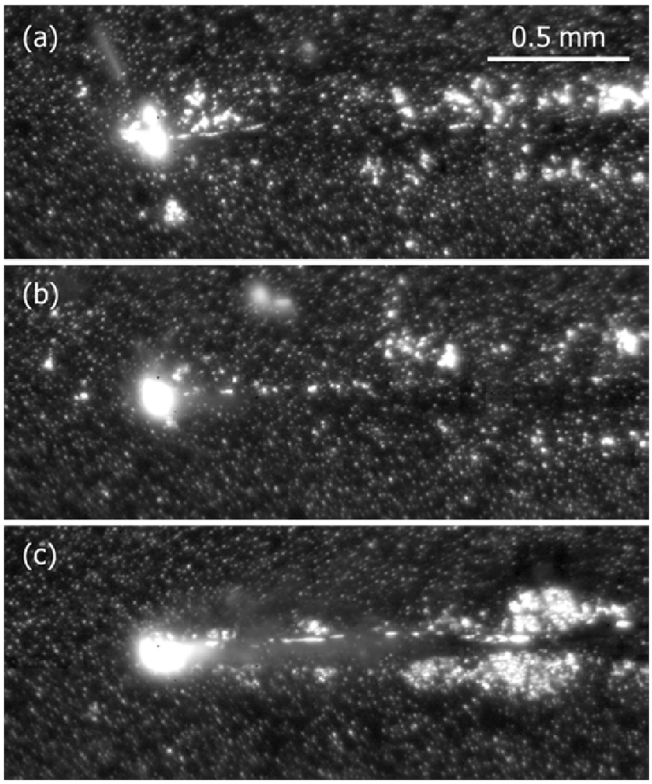

Fig. 2. High-speed images for top view when scanning single tracks (right to left scan direction) at 1 bar. Laser power and scan speeds of (a) 50 W and 0.2 m/s, (b) 100 W and 0.4 m/s and (c) 200 W and 0.8 m/s. The videos for all figures are included in the supplementary material.

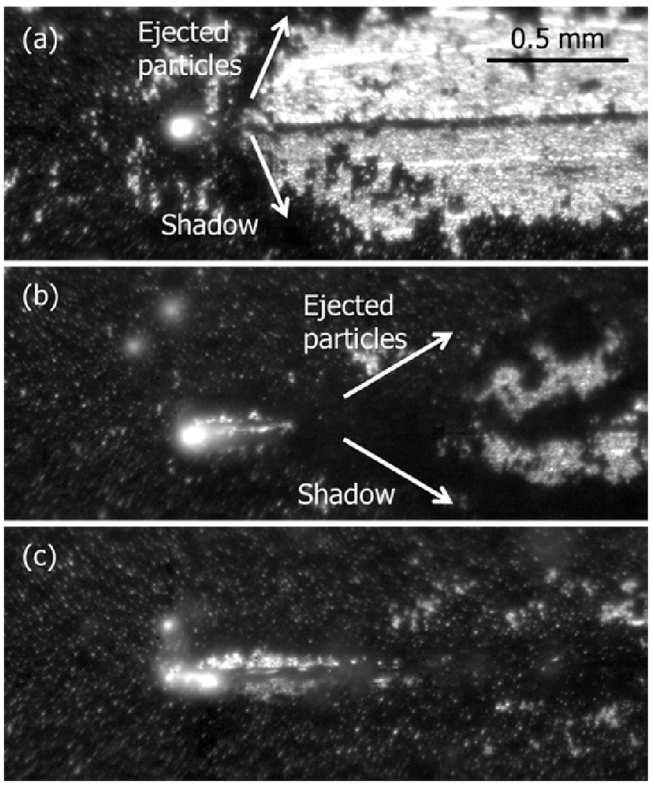

Fig. 3. High-speed images at 20 mbar. Laser power and scan speeds of (a) 50 W and 0.2 m/s, (b) 100 W and 0.4 m/s and (c) 200 W and 0.8 m/s.

energy (laser power divided by scan speed) of 250 J/m: 50 W and 0.2 m/s, 100 W and 0.4 m/s, and 200 W and 0.8 m/s. The 100 W laser power condition has been shown to build parts with > 99% density in our system [11]. All pressures reported are absolute, i.e. 1 bar corresponds to atmospheric pressure. High-speed images sequences were recorded for the 'top' view of the powder bed for single track laser scans.

Fig. 2 and Videos Fig. 2(a)-2(c) show baseline measurements recorded at 1 bar. The results are consistent with our previous observations at atmospheric pressure: both the direction of spatter ejection and the denudation mechanism change with different process parameters [12]. At the 50 W condition, Fig. 2(a), the laser plume is established forwards with respect to the laser scan direction. The induced flow of the ambient gas entrains powder particles in towards the melt pool from all directions on the powder bed, which are consolidated into the track or ejected forwards. At 100 W, Fig. 2(b), the plume and spatter are directed predominantly vertically upwards, resulting in less momentum in the shield gas flow at the powder level and consequently in less denudation. At 200 W, Fig. 2(c), the plume and spatter are directed backwards with respect to the scan direction, at a sufficiently low angle to impinge on the powder bed and to blow particles away from the track. Clearly the parameters at 200 W are not suitable due to the onset of balling. However, the higher frame rate used here (40,000 fps) compared to that used in the previous study (8000 fps in Ref. [12]) enabled the balling process to be observed directly, for the first time for PBF to the best of our knowledge. Molten metal from the melt track moves backwards into the 'ball'. Once the ball has solidified sufficiently, the next instability begins to receive molten material backwards from the melt pool, and the process repeats in a reasonably regular pattern.

Supplementary video related to this article can be found at http://dx.doi.org/10.1016/j.ijmachtools.2018.03.007.

Fig. 3 and Videos Fig. 3(a)-3(c) show the results recorded at 20 mbar. Despite the low pressure, a far larger number of powder particles are entrained in the flow induced by the laser plume, and they are drawn in from considerably further away on the bed. It is inferred that the vertical speed of the laser plume is larger than at 1 bar, but at the same time the inward flow begins to be offset by the lateral expansion of the laser plume that is associated with the transition to molecular flow. The flow transition with reduced pressure can be characterised by a Knudsen number $Kn \approx 1$, from a hydrodynamic flow where $Kn << 1$ to a molecular flow where $Kn >> 1$ [13]. The Knudsen number was of the order 0.018 and 0.9 at 1 bar and 20 mbar, respectively, assuming a temperature of 2000 K and particle diameter of 40 μm [5] and the dynamic viscosity and the atomic mass of Ar to be 89 kg/(ms) and 6.67×10^{-26} kg respectively. The dense jet of entrained particles casts a shadow on to the powder bed, due to the angle of illumination and observation. To understand the cause of this shadow, point P in Fig. 1(b) represents an entrained particle vertically above the laser scan line: in the camera image it appears above the scan line, whilst its shadow appears below the scan line. The jet of entrained particles and its shadow are marked in Fig. 3(a) and (b). The effect is most obvious for the highest scan speed once the laser beam has passed out of the field of view: the correlation between features in the jet of particles and its shadow are apparent, which can be observed in Video Fig. 3(c) and are labelled in a single frame in Fig. 4.

Supplementary video related to this article can be found at http://dx.doi.org/10.1016/j.ijmachtools.2018.03.007.

At 1 mbar, Fig. 5 and Videos Fig. 5(a)-5(c), powder particles are still drawn in from a considerable distance away on the powder bed. At the lowest scan speed, Fig. 5(a), the bare metal surface of the coupon is just visible in a distinct gap between the front of the melt pool and the powder in front of the track: the outward flow of the laser plume carries sufficient momentum to overcome the inward flow of entrained particles and to clear the laser track. The Knudsen number is approximately 18 and the flow is still in the transition region between the

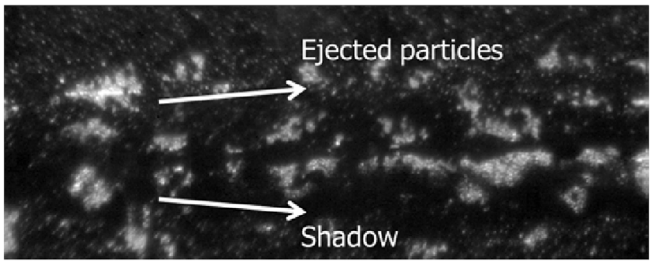

Fig. 4. High-speed image at 20 mbar for 200 W and 0.8 m/s. The symmetry of the entrained particles and their shadow are particularly clear when the laser spot has exited the field of view.

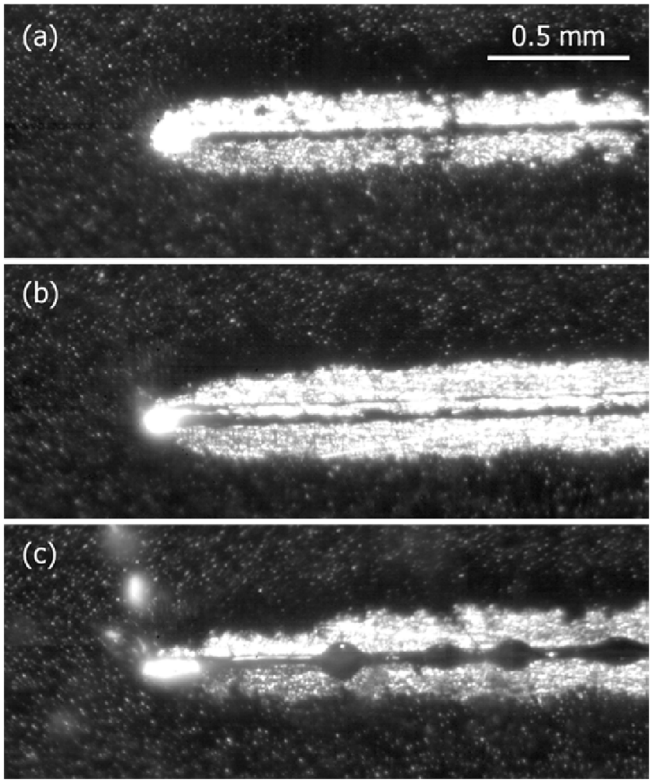

Fig. 5. High-speed images at 1 mbar. Laser power and scan speeds of (a) 50 W and 0.2 m/s, (b) 100 W and 0.4 m/s and (c) 200 W and 0.8 m/s.

hydrodynamic and molecular regimes. At 0.4 m/s, the scan speed of the laser matches more closely the speed at which particles are repelled by the vapour, whilst at 0.8 m/s the particles do not have sufficient speed to escape and are still incorporated into the melt pool. The laser scan speed is acting cumulatively with the inwards drag forces exerted on particles by the induced ambient flow, whilst competing with the vapour expansion velocity which repels particles from the melt pool.

Supplementary video related to this article can be found at http://dx.doi.org/10.1016/j.ijmachtools.2018.03.007.

Finally, at 10 µbar, Fig. 6 and Videos Fig. 6(a)-6(c), no inward flow of entrained particles from the powder bed is observed and the flow has become fully molecular, $Kn \approx 1800$. The outward flow of particles directly affected by the laser plume at 0.2 and 0.4 m/s is slightly increased with respect to 1 mbar, indicating that the velocity of the plume in the plane of the powder bed has increased between the two pressures. However, the 0.8 m/s scan speed is still sufficiently fast to prevent particles escaping the melt pool.

Supplementary video related to this article can be found at http://dx.doi.org/10.1016/j.ijmachtools.2018.03.007.

Typical track profiles are shown in Fig. 7. These are presented

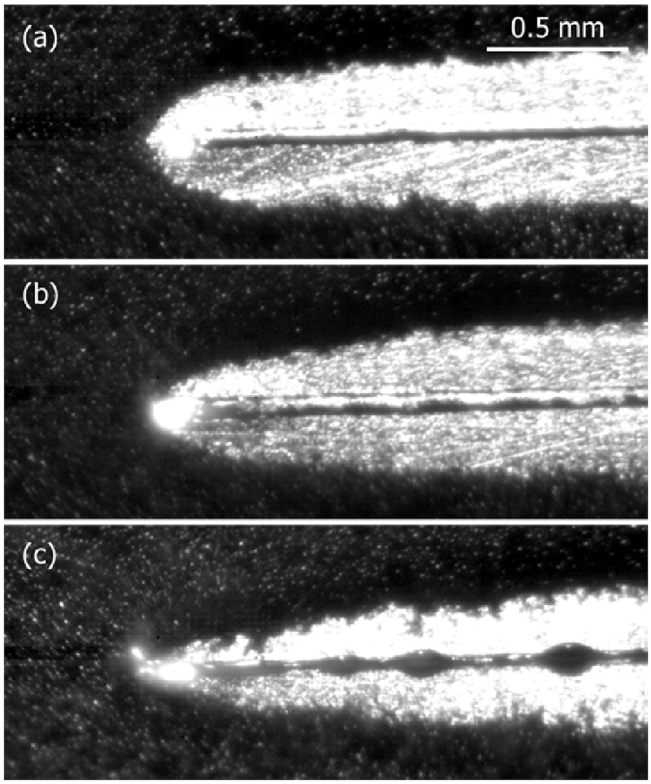

Fig. 6. High-speed images at 10 µbar. Laser power and scan speeds of (a) 50 W and 0.2 m/s, (b) 100 W and 0.4 m/s and (c) 200 W and 0.8 m/s.

according to laser processing condition in order to observe the effect of pressure in each case. At 50 W and 0.2 m/s, Fig. 7(a), the cross-sectional area of the bead is significantly reduced at 20 mbar and below. It is clear from Figs. 5(a) and 6(a), and the associated videos, that the profiles at 1 mbar and 10 µbar are melted substrate and do not contain any powder. The profile at 20 mbar similarly contains almost no powder, despite the large entrainment of powder towards the melt-pool. Of the pressures tested, 20 mbar was apparently on the cusp of these entrained particles being expelled by the expansion of the laser plume, for the 50 W condition. The profiles for 100 W and 0.4 m/s, Fig. 7(b), are also significantly reduced at pressures below 1 bar, although slightly larger than for 50 W and 0.2 m/s: the front of the melt pool and the powder always interact, even at 10 µbar. Finally, Fig. 7(c) shows the profiles for the 200 W and 0.8 m/s. Powder is incorporated into the melt pool at all pressures due to the high scan speed, although balling occurs in each case and is not a suitable process setting for a PBF build.

Typical track cross-sections are shown in Fig. 8. In general the penetration increased with a decrease in ambient pressure but became independent of pressure at some threshold pressure above 20 mbar.

4. Discussion

The results show that the reduced bead profile in single-layer tracks at sub-atmospheric pressure is primarily due to increased denudation, rather than increased metal vaporization as reported previously [2,3]. The apparent contradiction between these two references regarding suggested processing parameters at sub-atmospheric pressures is resolved: it is most likely that the 100% density reported at 100 µbar and very low scan speeds ≤ 0.02 m/s [2] was in fact measured from the coupon substrate which had been completely cleared of powder, under conditions similar to Fig. 6(a). We have scanned islands at these pressures, Fig. 9(a) and Video Fig. 9(a), and it is clear that the substrate is cleared of powder throughout the scan and that no powder is

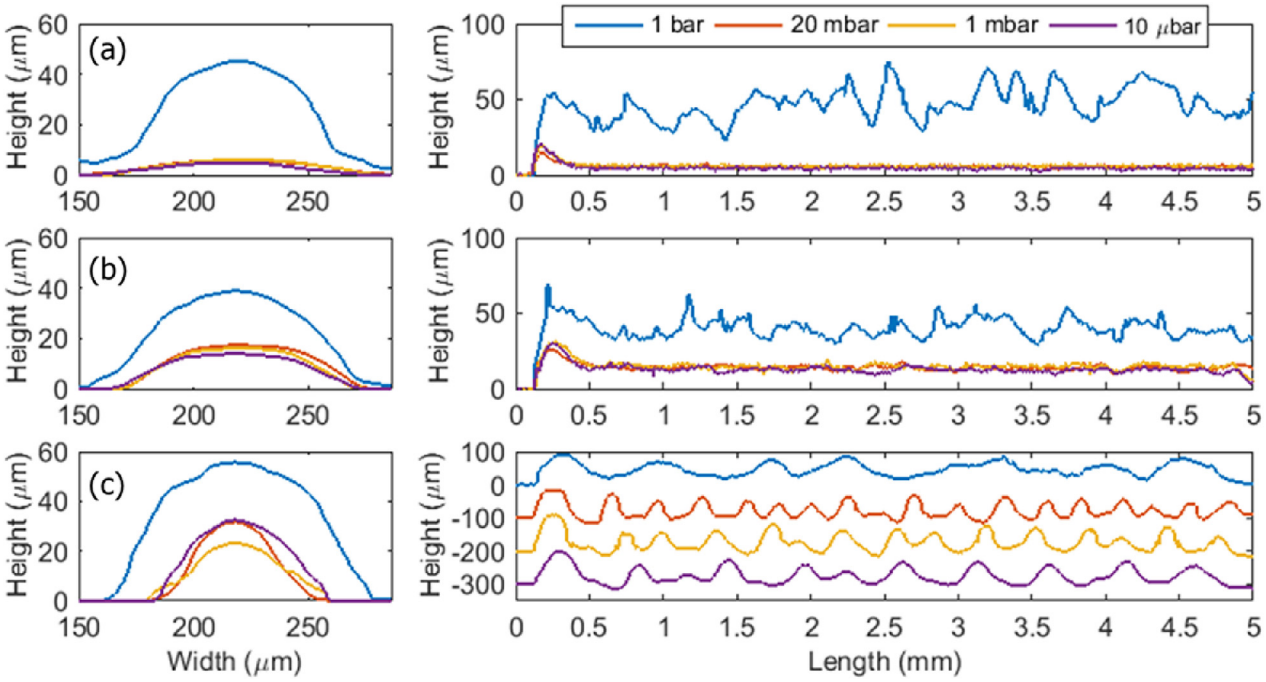

Fig. 7. Transverse (left-hand column) and longitudinal (right-hand column) profiles of the laser tracks. Laser power and scan speeds of (a) 50 W and 0.2 m/s, (b) 100 W and 0.4 m/s and (c) 200 W and 0.8 m/s.

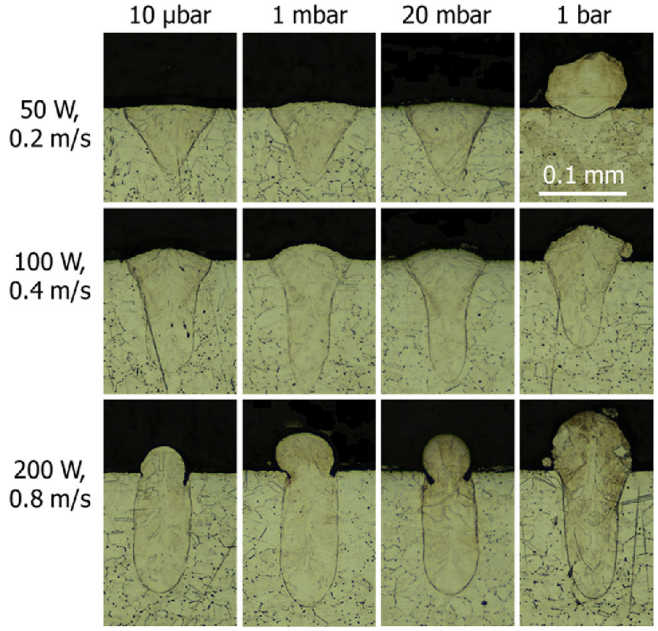

Fig. 8. Cross-sections of laser tracks.

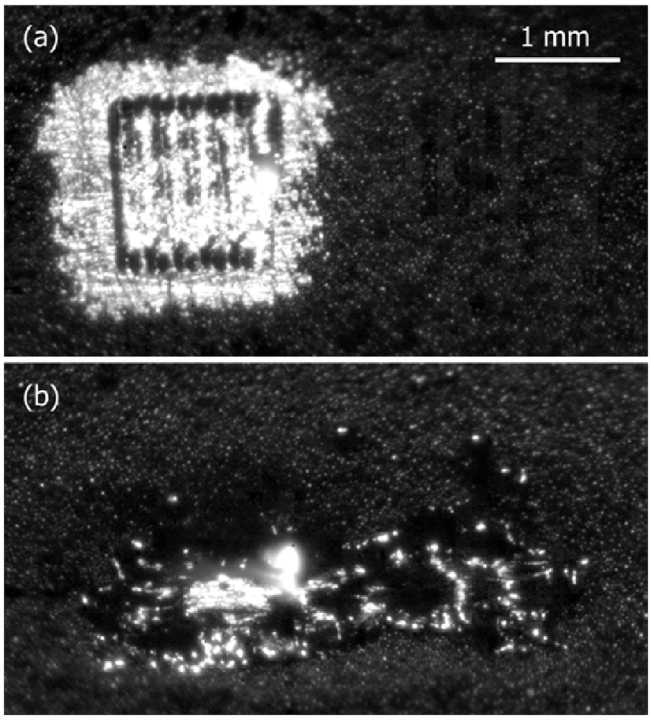

Fig. 9. Top view of island scans for (a) 50 μm powder layer spread on baseplate at 10 μbar for 50 W and 0.1 m/s and (b) 130 μm powder layer spread on a PBF surface at 10 μbar for 100 W and 0.4 m/s.

incorporated. It also explains why the measured density decreased steadily to 70% as the laser scan speed was increased to 0.6 m/s [2]: powder was eventually incorporated into the track by conditions similar to Fig. 6(b) and (c).

Supplementary video related to this article can be found at http://dx.doi.org/10.1016/j.ijmachtools.2018.03.007.

The observation by the same group that no powder was consolidated below 100 mbar at 0.1 m/s scan speed [3] is consistent with the results reported here, for example the track profiles shown in Fig. 7(a). However, simply increasing the scan speed (or a reducing the power) of the laser [3] does not inform the choice of process parameters: the results presented here show that unwanted balling can indeed occur at high scan speeds, even for sub-atmospheric pressures.

The extremely low surface roughness and lack of spatter observed at 50 nbar and 10 mm/s [4] is again most likely due to measurements made from the coupon substrate, which had been completely cleared of powder. Indeed, a previous publication by the same group includes images of these low roughness surfaces which are completely devoid of any residual powder [14]. It also explains why they observed both the

surface roughness and spatter to increase at 100 mm/s: powder was eventually incorporated into the track by conditions similar to Fig. 6(b) and (c). The appearance of spatter as the laser scan speed increases and eventually incorporates powder into the track is evident when comparing Video Figs. 6(a) and (c), for example.

Fig. 9(a) showed how the powder is cleared from the substrate during area scans at low pressure (10 µbar). This image is for a powder layer thickness of 50 µm spread directly on to the baseplate for which the denudation is greatest. The effect of denudation is reduced as the steady state build condition is reached, due to the increase in the powder layer thickness [11] and surface irregularities of previously built layers constraining the particle motion [12]. Fig. 9(b) and Video Fig. 9(b) show the laser interacting at 10 µbar with a 130 µm thick powder layer spread on to a PBF surface (built under standard atmospheric conditions). Even under these conditions, which are representative of the steady build state, the substrate is cleared by the outward expansion of the evaporation plume.

The videos provide the first direct observation of the outward expansion of the evaporation plume counter-acting and eventually dominating any inward flow of the ambient gas as the pressure decreases, for example Figs. 3(a) and 5(a) and 6(a) for the 50 W condition. They confirm that denudation due to asymmetrical heating of particles close to the laser spot being propelled away by the vapour flux generated, was correctly discounted in Ref. [5]. The pressures at which the flow regime transitions from hydrodynamic to molecular, and the trends in the resulting denudation, are also generally consistent with those inferred from measurements of the size of the denuded region.

Fig. 8 showed an increase in penetration depth with reduced pressure. This increase is attributed to the reduction in vaporization temperature at low pressure, similar to that observed in laser keyhole welding. The Clapeyron equation describes the gradient of the coexistence curve on the phase diagram of a material, for which two phases exist in thermodynamic equilibrium, $dP/dT = L/(T\ \Delta v)$, where P is the pressure, T is the absolute temperature and Δv and L are the change in specific volume and the latent heat of the phase transition, respectively. For vaporization well below the critical point, the change in specific volume of the vapour is significantly larger than that of the liquid, enabling the specific volume to be replaced using the ideal gas law to obtain the Clausius-Clapeyron equation [2,3]:

$$\ln\left(\frac{P_2}{P_1}\right) = \frac{L_{vap}}{R}\left(\frac{1}{T_1} - \frac{1}{T_2}\right) \tag{1}$$

where R is the specific gas constant and (P_1, T_1) and (P_2, T_2) are two points on the phase boundary. The change in vaporization temperature with ambient pressure is plotted in Fig. 10 for stainless steel 316 L, taking the boiling point of 3090 K at atmospheric pressure and the latent heat of vaporization, L_{vap} = 7.45 MJ/kg. The plot also includes the empirical line:

$$\log(P) = 11.1183 - \frac{18{,}868}{T} \tag{2}$$

which is determined from a fit to experimental data in the range 1750–5000 K [15,16] with the pressure in Pa. The melting point is essentially independent of pressure, and the $T_{liquidus}$ is marked on the figure. The pressures for the experiments reported here are marked in Fig. 10 and the lowest pressure is just above the sublimation region.

For laser welding at low speeds, the threshold pressure below which there is no noticeable effect on the penetration depth has been approximated at ~ P_c/10, where $P_c = \sigma/r$ is the pressure in the keyhole due to surface tension, σ, and r is the radius of the keyhole [8]. A plot of the variation in surface tension with temperature for stainless steel 316 L is given in Ref. [17] from which the approximate relation for surface tension (in N/m) of $\sigma = -0.45 \times 10^{-3}T + 2.65$ was determined in the temperature range 2000 to 4000 K. Using the vaporization temperature at 1 bar from Fig. 10, combined with an approximate keyhole radius of 25 µm from Fig. 8, yields a threshold pressure of 50 mbar. This

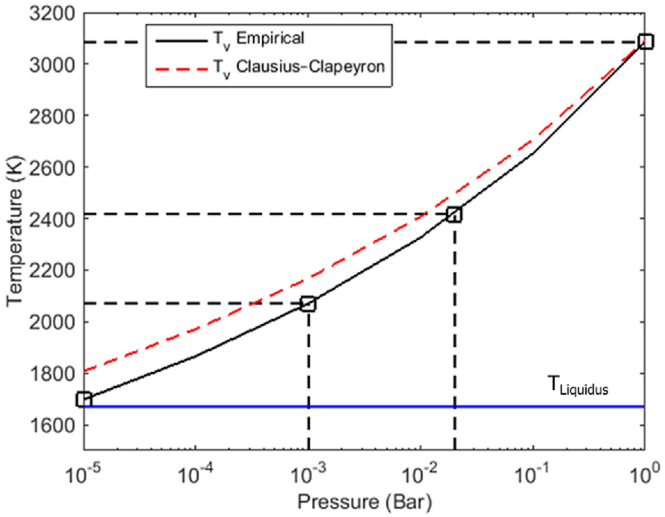

Fig. 10. Plot of vaporization temperature against pressure. The pressures reported here are marked and the corresponding vaporization temperatures are: 1698 K at 10 µbar; 2071 at 1 mbar; 2415 K at 20 mbar and 3087 K at 1 bar.

estimate applies to low weld speeds [6], so in practice the threshold pressure is likely to be somewhat higher for PBF because the higher laser scan speed will make a small pressure contribution in addition to the surface tension pressure. This estimate of the threshold pressure requires further experiments to be validated, but it is consistent with Fig. 8 where the deepest penetration has already been reached by 20 mbar.

The reduced vaporization temperature and its effect on the surface tension also appears to affect the balling frequency seen at the highest scan speed. A fast-Fourier transform of the longitudinal scan profiles in Fig. 7(c) yielded the balling spatial frequency, from which the typical length between balls was calculated. The vaporization temperature plotted against this balling length shows a linear relationship, Fig. 11. The balling length is considerably shorter than predicted for a Plateau-Rayleigh instability [18]: the melted substrate shown in the cross-sections in Fig. 8 indicate that the mechanism was not a molten 'cylinder' breaking into droplets. A Kelvin-Helmholtz hydrodynamic instability can arise when the velocity of the liquid metal at the surface of the melt-pool is lower than the velocity of the atmosphere [19] but this effect is less well understood and it is not straightforward to predict the

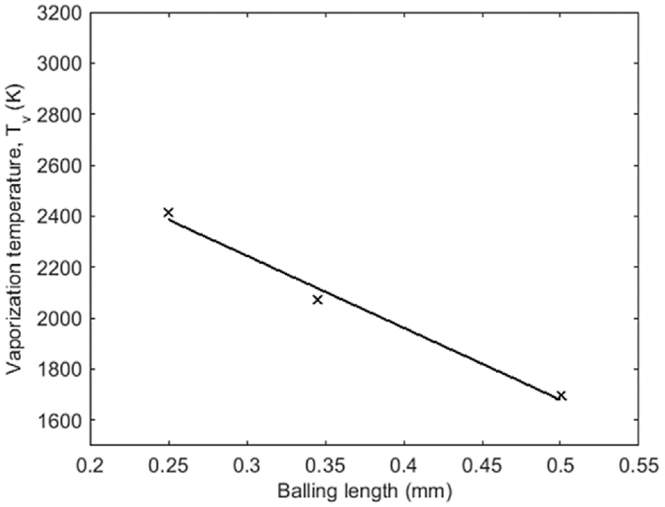

Fig. 11. Vaporization temperature (which is linearly related to surface tension in this temperature range [17]) plotted against distance between balls from Fig. 7(c).

balling length from the process parameters.

These results and observations lead to some guidance for exploring potential PBF at sub-atmospheric pressures. Operating in a soft vacuum in the hydrodynamic regime would provide the simplest implementation. In that case, there is no benefit in reducing the pressure below the threshold at which the penetration depth no longer increases (~50 mbar): the disruption to the powder bed increases with no gain in penetration. The reduction in vaporization temperature at reduced pressure means that the same penetration depth can be achieved at a lower laser power: reduced laser power has a stabilizing effect on the process [12] and reduced thermal input to the powder bed. The laser power could possibly be reduced even further if less penetration depth is required due to an associated reduction in porosity: potentially only 1–2 layers would need to be re-melted for each track rather than the 3–4 layers in the typical PBF process. If the disruption to the powder bed remains too great in this hydrodynamic regime above 50 mbar, even with the potential reduction in laser power, a pre-sinter analogous to e-beam PBF might be required. However, the hard vacuum (nbar) and x-ray production associated with the e-beam technique would be avoided. Clearly a reduction in porosity in the built part should be critical for its intended use if the additional processing time and increase in process complexity associated with a pre-sinter are to be tolerated. If lower pressures in the transition or molecular flow regimes are to be used, a pre-sinter would be essential to maintain the integrity of the powder bed.

5. Conclusions

The reduced bead profiles seen in single-layer tracks at sub-atmospheric pressure are primarily due to increased denudation, rather than increased metal vaporization. As the pressure decreases in the transition region between hydrodynamic and molecular flows, entrainment of particles towards the melt pool increases but is in competition with the repelling of particles away from the melt pool by the expansion of the laser plume. Eventually, in the molecular flow regime, particles are only repelled by the plume away from the melt pool. The resulting disruption to the powder bed means that most pressures would require a pre-sinter for the process to be viable, with a corresponding increase in processing time and complexity. The regime between 1 bar and ~50 mbar (the threshold pressure at which the penetration depth no longer increases) could provide an interesting window for processing without a pre-sinter, but further investigation is required.

Acknowledgements

This work was supported by the Engineering and Physical Sciences Research Council (Grant number EP/K030884/1). The authors are grateful to Jolyon Cleaves of Vision Research for use of the Phantom V2512 high-speed camera, and to Toby Scrivener of Laser 2000 (UK) Ltd. for use of the Lumencor SOLA SM light engine.

References

[1] I. Gibson, D.W. Rosen, B. Stucker, Additive Manufacturing Technologies, Springer, Boston, MA, 2010.
[2] B.C. Zhang, H.L. Liao, C. Coddet, Microstructure evolution and density behavior of CP Ti parts elaborated by Self-developed vacuum selective laser melting system, Appl. Surf. Sci. 279 (2013) 310–316.
[3] A. Masmoudi, R. Bolot, C. Coddet, Investigation of the laser-powder-atmosphere interaction zone during the selective laser melting process, J. Mater. Process. Technol. 225 (2015) 122–132.
[4] Y. Sato, M. Tsukamoto, S. Masuno, Y. Yamashita, K. Yamashita, D. Tanigawa, N. Abe, Investigation of the microstructure and surface morphology of a Ti6Al4V plate fabricated by vacuum selective laser melting, Appl. Phys. Mater. Sci. Process 122 (4) (2016) 439.
[5] M.J. Matthews, G. Guss, S.A. Khairallah, A.M. Rubenchik, P.J. Depond, W.E. King, Denudation of metal powder layers in laser powder bed fusion processes, Acta Mater. 114 (2016) 33–42.
[6] Y. Arata, N. Abe, T. Oda, Fundamental phenomena in high power CO2 laser (Report II) – vacuum laser welding, Trans. JWRI 14 (2) (1985) 17–22.
[7] S. Katayama, A. Yohei, M. Mizutani, Y. Kawahito, Development of deep penetration welding technology with high brightness laser under vacuum, Proceedings Lasers in Manufacturing (LIM), Physics Procedia 12 Part A, 2011, pp. 75–80.
[8] R. Fabbro, K. Hirano, S.Y. Pang, Analysis of the physical processes occurring during deep penetration laser welding under reduced pressure, J. Laser Appl. 28 (2) (2016) 022427.
[9] A. Verwaerde, R. Fabbro, G. Deshors, Experimental study of continuous CO2-laser welding at subatmospheric pressures, J. Appl. Phys. 78 (5) (1995) 2981–2984.
[10] Y. Kawahito, K. Kinoshita, N. Matsumoto, S. Katayama, Visualization of refraction and attenuation of near-infrared laser beam due to laser-induced plume, J. Laser Appl. 21 (2) (2009) 96–101.
[11] P. Bidare, R.R.J. Maier, R.J. Beck, J.D. Shephard, A.J. Moore, An open-architecture metal powder bed fusion system for in-situ process measurements, Addit. Manuf. 16 (2017) 177–185.
[12] P. Bidare, I. Bitharas, M. Ward, M.M. Attallah, A.J. Moore, Fluid and particle dynamics in laser powder bed fusion, Acta Mater. 142 (2018) 107–120.
[13] G.A. Bird, Molecular Gas Dynamics and the Direct Simulation of Gas Flows, Oxford University Press, Oxford, 1994.
[14] Y. Sato, M. Tsukamoto, Y. Yamashita, Surface morphology of Ti-6Al-4V plate fabricated by vacuum selective laser melting, Appl. Phys. B Laser Optic. 119 (3) (2015) 545–549.
[15] C.S. Kim, Thermophysical Properties of Stainless Steels, ANL-75–55, Argonne National Laboratory, USA, 1975.
[16] International Atomic Energy Agency (IAEA), Thermophysical Properties of Materials for Nuclear Engineering: a Tutorial and Collection of Data, (2008).
[17] H. Ki, P.S. Mohanty, J. Mazumder, Modeling of laser keyhole welding: Part I. Mathematical modeling, numerical methodology, role of recoil pressure, multiple reflections, and free surface evolution, Metall. Mater. Trans. 33A (2002) 1817–1830.
[18] I. Yadroitsev, A. Gusarov, I. Yadroitsava, I. Smurov, Single track formation in selective laser melting of metal powders, J. Mater. Process. Technol. 210 (12) (2010) 1624–1631.
[19] T. DebRoy, H.L. Wei, J.S. Zuback, T. Mukherjee, J.W. Elmer, J.O. Milewski, A.M. Beese, A. Wilson-Heid, A. Ded, W. Zhang, Additive manufacturing of metallic components – Process, structure and properties, Prog. Mater. Sci. 92 (2018) 112–224.